Journal of Zhejiang University-SCIENCE A (Applied Physics & Engineering)
www.jzus.zju.edu.cn; www.springer.com/journal/11582
E-mail: jzus_a@zju.edu.cn

Review

https://doi.org/10.1631/jzus.A2300660

Advances in halide perovskite semiconductors for energy-integrated and energy-resolved X-ray detection

Yibin LAI, Yang (Michael) YANG✉

State Key Laboratory of Modern Optical Instrumentation, Institute for Advanced Photonics, College of Optical Science and Engineering, Zhejiang University, Hangzhou 310027, China

Abstract: X-ray and γ-ray detectors are widely used in medical, military, security, material analysis, and industrial inspection. In recent years, perovskite materials have become promising materials for radiation detection owing to their strong stopping power, considerable carrier transportation ability, and simple synthesis process. Previous studies have demonstrated both direct and indirect radiation detectors using perovskite materials. In this review, we aim to elucidate the mechanism by which X-rays and γ-rays interact with matter, explain the principles of the energy integrating mode and photon counting mode for direct detection, and discuss the key factors determining device performance. Furthermore, we summarize recent advances in perovskite-based radiation detectors for both modes. Additionally, we identify challenges that need to be overcome to enable perovskite materials to be successfully commercialized.

Key words: Halide perovskite; X-ray; Direct detection; Photo counting

1 Introduction

X-rays and γ-rays with energies between tens of kilo and mega electron volts have broad applications, including medical examination (van Eijk, 2002; Spahn, 2013), industrial monitoring (Kalaga et al., 2009; Kim J et al., 2012), and security screening (Zentai, 2008). It is imperative to keep the radiation dose as low as possible, especially in medical examinations, because high-dose radiation increases the risk of cancer (Lin, 2010), endangering people's health. Hence, detectors with both high sensitivity and a low detection limit are crucial to minimize the used radiation dose.

Widely used semiconductor materials for these applications include CdTe/CdZnTe (CZT) (del Sordo et al., 2009), amorphous selenium (a-Se) (Safa et al., 2011), and silicon (Guerra et al., 2012). However, each material has specific challenges that degrade its device performance. Fabrication of large-area wafers poses a significant challenge for CdTe/CdZnTe, while a-Se suffers from poor sensitivity and stability. Silicon has a low absorption efficiency compared to other materials.

In recent years, halide perovskites have been extensively researched and applied in various fields owing to their remarkable photoelectric properties. Initially, they were used as absorbers in solar cells (Kojima et al., 2009). Since Kim HS et al. (2012) reported perovskite solar cells with an efficiency of 9.7% in 2012, halide perovskite materials have gained extensive attention, with applications extending to light-emitting diodes (LEDs) (Tan et al., 2014), lasers (Xing et al., 2014), and radiation detectors (Yakunin et al., 2015). There are two methods for radiation detection, direct detection and indirect detection. Halide perovskites exhibit appealing device performance in direct detection due to their strong radiation stopping power, low dark current, high sensitivity, and simple synthesis.

In this review, we focus on direct detection based on halide perovskites. First, we introduce the distinct processes X-rays and γ-rays undergo when the photons interact with detectors. Then, we elucidate the working principles of direct detection. Two types of

✉ Yang (Michael) YANG, yangyang15@zju.edu.cn
Yibin LAI, https://orcid.org/0000-0003-3511-6970
Yang (Michael) YANG, https://orcid.org/0000-0002-3362-7155

Received Dec. 29, 2023; Revision accepted Mar. 12, 2024; Crosschecked Apr. 27, 2024

direct detection detectors are discussed: energy integrating detectors (EIDs) and photon counting detectors (PCDs). Additionally, we systematically review progress in the development of EIDs and PCDs. Lastly, we summarize the challenges that must be overcome to enable the successful commercialization of perovskite materials.

2 Interaction of X-rays and γ-rays with matter

Fig. 1a depicts the various mechanisms by which X-rays interact with matter, including photoelectric absorption, scattering, and pair production. During X-ray detection, these mechanisms convert either the total or a portion of the energy from an X-ray photon into electron-hole pairs. The electron-hole pairs are then collected by the read-out circuit, producing electrical signals.

2.1 Photoelectric absorption

In the process of photoelectric absorption, a semiconductor atom completely absorbs the X-ray photon. The energy of an X-ray photon is transferred to one of the bound electrons in a certain orbit of the atom, which leads to the ejection of the bound electron with

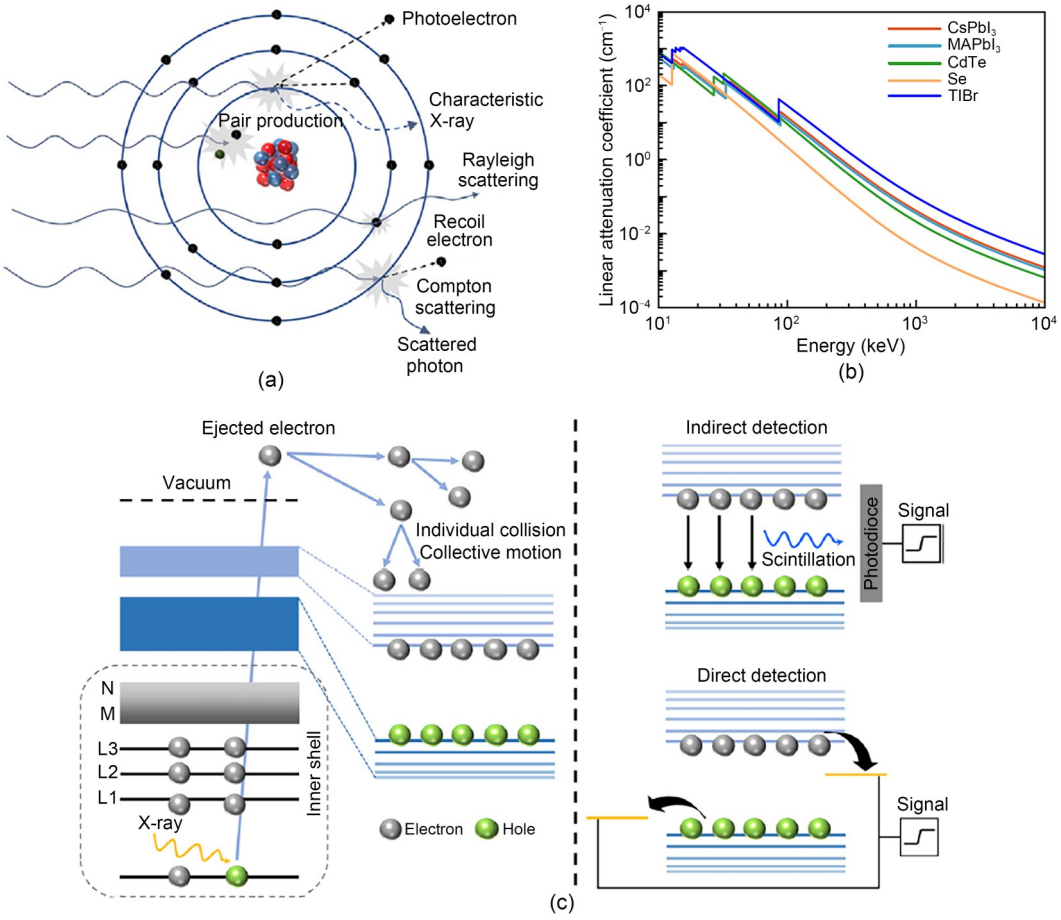

Fig. 1 (a) Processes by which X-ray (γ-ray) photons interact with matter: photoelectric absorption, Rayleigh scattering, Compton scattering, and pair production; (b) Linear attenuation coefficient for various materials (MA is methylammonium); (c) Mechanism of electron-hole generation in semiconductors under X-rays (γ-rays) and the mechanisms of indirect and direct detections. Electrons at the inner shell escape after absorbing X-rays (γ-rays). Thousands of low-energy electrons are released through ionization during the escaped electrons transporting in the material. These low-energy electrons are rapidly thermalized to the bottom of the conduction band to form electron-hole pairs. In indirect detection, electron-hole pairs recombine to emit visible light. In direct detection, electrons and holes are collected by electrodes under an applied electric field. Figs. 1a and 1c are reprinted from (Wu et al., 2021), Copyright 2021, with permission from Elsevier. Fig. 1b is reprinted from (Wei and Huang, 2019), Copyright 2019, with permission from Springer Nature. References to color refer to the online version of this figure

a specific energy. The energy of the escaped photoelectron is given by the following equation (Evans and Beiser, 1956):

$$E_e = hv - E_k, \tag{1}$$

where hv is the energy of the X-ray photon and E_k is the binding energy of the escaped photoelectron. Upon the escape of the electron, a hole is created at its original position. This hole quickly undergoes rearrangement by capturing free electrons or electrons in other shells of the atom. This rearrangement process is accompanied by the generation of one or several characteristic X-ray photons.

The atomic attenuation coefficient of photoelectric absorption (χ) satisfies the following equation (Kainz, 2006):

$$\chi \propto \frac{Z^4}{(hv)^3}, \tag{2}$$

where Z is the average atomic number of the semiconductor material. Therefore, the photoelectric absorption is dominant when the energy of the X-ray photon is low. Moreover, the probability of photoelectric absorption increases when the average atomic number of the semiconductor material becomes larger.

2.2 Scattering

X-ray scattering comprises Rayleigh scattering and Compton scattering. Rayleigh scattering is a coherent and elastic process, indicating that the energy of the X-ray photons remains unchanged. The propagation direction of the X-ray photons is only slightly deflected after Rayleigh scattering. In contrast, Compton scattering is incoherent and inelastic. The X-ray photons that undergo Compton scattering transfer some of their energy to the colliding electrons and the X-ray photons are deflected by an angle after the scattering. The energy lost by the X-ray photons varies with the scattering angle: as the scattering angle increases, the loss of energy from the X-ray photons decreases.

The atomic attenuation coefficient of Compton scattering (δ) follows the relationship below (Kainz, 2006):

$$\delta \propto Z. \tag{3}$$

Hence, this probability increases linearly with the average atomic number of the semiconductor material. Furthermore, for a given scattering angle, the scattering becomes progressively more inelastic as the energy of the incident X-ray photon increases (Als-Nielsen and McMorrow, 2011). This implies that Compton scattering becomes dominant when the energy of the X-ray photon is high.

2.3 Pair production

Pair production becomes possible only when the X-ray photon exceeds 1.02 MeV ($2m_ec^2$, where m_e is the still mass of the electron and c is the light velocity). The photon produces an electron-positron pair under the Coulomb field of either a nucleus or orbital electron (Hendee, 2010). The part of the energy that exceeds 1.02 MeV is equally divided into the kinetic energy of the electron and positron. As positrons are readily annihilated after moderation in the semiconductor material, this process typically results in the production of two annihilation photons. The atomic attenuation coefficient of pair production (κ) is roughly proportional to the square of the atomic number ($\kappa \propto Z^2$).

2.4 Linear absorption coefficient

To assess the overall probability of incident X-ray photons being absorbed by the semiconductor material, the linear absorption coefficient (μ_0) is introduced. The linear absorption coefficient is the sum of χ, δ, and κ:

$$\mu_0 = \chi + \delta + \kappa. \tag{4}$$

The mass attenuation coefficient (α) is defined as the linear absorption coefficient divided by the material density (ρ):

$$\alpha = \frac{\mu_0}{\rho} = \frac{\chi}{\rho} + \frac{\delta}{\rho} + \frac{\kappa}{\rho}. \tag{5}$$

In the case where the semiconductor material is a mixture or compound, the linear absorption coefficient is the sum of the products of the mass attenuation coefficient for each element and its mass percentage (Leroy and Rancoita, 2011). Fig. 1b shows the linear absorption coefficients for some materials. The transmitted photon flux intensity (I) follows a relationship

of $I=I_0\times e^{-\mu_0 l}=I_0\times e^{-\alpha\rho l}$, where I_0 is the initial photon flux intensity and l is the length of the absorber (Wei and Huang, 2019).

3 Direct detection of X-rays and γ-rays

X-ray detectors can be categorized into two types based on their working principles: direct detection and indirect detection. As depicted in Fig. 1c, when X-ray photons are incident into the semiconductor, whether by direct detection or indirect detection, they are absorbed by photoelectric absorption, Compton scattering, or pair production, generating electron-hole pairs. In direct detection, the electrons and holes are transported under an applied electric field and collected by electrodes to generate an electrical signal. During indirect detection, electrons at the bottom of the conduction band and holes at the top of the valence band recombine to emit fluorescence. A photodetector collects the fluorescence at the back end to generate an electrical signal.

3.1 Mechanism of direct detection

Direct detection has two available working modes: the energy integrating mode and the photon counting mode. The difference between these two modes lies in that EIDs integrate the total energy deposited in the detectors without identifying the number and energy of X-ray photons, while PCDs are capable of discriminating the energy of each incident photon. Nevertheless, the mechanism of X-ray photon absorption and generation of electron-hole pairs is the same for both. In direct detection, incident X-ray photons are first absorbed by photoelectric absorption or Compton scattering. The ejected hot-electron leaves a hole in the valence band (Wu et al., 2021) and generates highly energetic secondary electrons, such as photoelectrons, Auger electrons, and recoil electrons (Wu et al., 2021). Thousands of low-energy electrons are released through ionization during the transport of escaped electrons in the material and rapidly thermalized to the bottom of the conduction band to form electron-hole pairs. Electrical signals are generated by applying an electric field to collect charges.

The ionization energy (Δ), which is the energy required for a semiconductor to generate an electron-hole pair, is a critical parameter determining detection efficiency. It makes it possible to calculate the number of electron-hole pairs based on the incident X-ray dose, provided that the detector fully absorbs the photons. The ionization energy is closely related to the bandgap (E_g) of the semiconductor material. According to Devanathan et al. (2006), the ionization energy of the direct detection material can be calculated by an empirical relation:

$$\Delta=2E_g+1.43. \tag{6}$$

In the case of indirect detection, Rothwarf (1973) derives $\Delta=2E_g$ by plasmon theory.

3.2 Energy integrating detectors (EIDs)

Energy integrating X-ray detectors operate in current mode and are commonly used for dose rate or clinical computed tomography (CT) measurement. In these application scenarios, the X-ray dose is relatively large to generate a high signal-to-noise ratio. As depicted in Fig. 2a, many X-ray photons are incident in the detector during each measurement interval, producing thousands of electron-hole pairs. In Fig. 2b, a thin-film transistor (TFT) containing a storage capacitor is required to store the collected charge and process the signal. To achieve low dose imaging for radiation safety, it is crucial for EIDs to have a low detection limit. According to the International Union of Pure and Applied Chemistry (IUPAC), the detection limit is the dose rate that produces a signal three times larger than the noise (Thompson et al., 2002). Consequently, EIDs with high sensitivity and low dark current are advantageous for acquiring a low detection limit.

3.2.1 Sensitivity

Sensitivity reflects the efficiency with which a detector converts incident X-ray photons into collectable charges and is calculated as (Kasap, 2000):

$$S=\frac{Q}{AD}, \tag{7}$$

where Q is the collected charges, A is the effective area of the detector, and D is the X-ray dose. Three main factors influence the sensitivity. The first is the X-ray absorption efficiency of the material, also known as the X-ray stopping power of the material. The linear absorption coefficient (μ_0) is often used to characterize

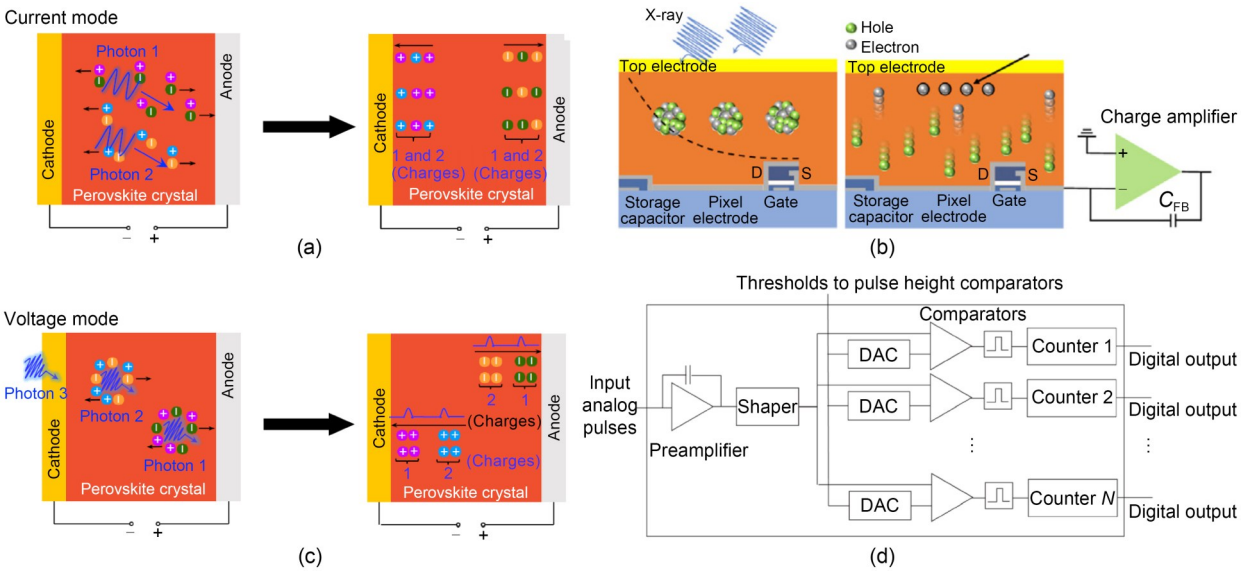

Fig. 2 (a) Mechanism by which EIDs work in the current mode (multiple photons reach the detector during one measurement interval; electron-hole pairs generated by different photons are collected to generate a signal); (b) Device configuration of EIDs (electrons are collected by the top electron and holes are collected by the storage capacitor; C_{FB} is the capacitance); (c) Mechanism by which PCDs work in voltage mode (the X-ray photons reach the detector one by one; each incident photon generates a number of electron-hole pairs that produce an electrical signal pulse); (d) Schematic diagram of the application-specific integrated circuit (ASIC) (the input signal is firstly processed by a preamplifier and a shaper, and then the amplified signal is compared in several comparators; if the signal exceeds the threshold, the corresponding counter counts the signal once). DAC is the digital-to-analog converter. Figs. 2a and 2c are reprinted from (Wei and Huang, 2019), Copyright 2019, with permission from Springer Nature. Fig. 2b is reprinted from (Wu et al., 2021), Copyright 2021, with permission from Elsevier. Fig. 2d is reprinted from (Taguchi and Iwanczyk, 2013), Copyright 2013, with permission from John Wiley & Sons, Inc. References to color refer to the online version of this figure

the X-ray stopping power of a material per unit thickness under certain photon energy (Su et al., 2020). As outlined in Section 2, the linear absorption coefficient is determined by the atomic number (Z) and density (ρ) of the material. Materials with high Z and large ρ consistently exhibit a high linear absorption coefficient. While a thicker semiconductor layer is needed to enhance X-ray utilization, it poses challenges that limit sensitivity. Charge collection efficiency (CCE) drops when the semiconductor layer becomes too thick, resulting in a low sensitivity (Safa et al., 2011). Thus, the materials for X-ray detectors need to have high Z and large ρ to ensure enough X-ray absorption efficiency without making the semiconductor layer too thick. Perovskite materials have a larger average atomic number than conventional X-ray detection materials such as a-Se and CZT, making them more suitable for X-ray detection. The second factor affecting sensitivity is the efficiency of generating electron-hole pairs, which can be calculated from the ionization energy (Δ). The number of free charges can be calculated as follows:

$$N=\frac{E}{\Delta}, \tag{8}$$

where E is the total energy absorbed by the EIDs. Therefore, semiconductor materials with low ionization energy are essential for X-ray detectors. As mentioned in Section 3.1, the ionization energy can be estimated by $\Delta=2E_g+1.43$ for direct detection. Most perovskite materials have an ionization energy of 5–6 eV, making them suitable for X-ray detection. The third factor is CCE. The process of charge transportation and collection is complicated and several parameters affect this process. Among these parameters, the product of carrier mobility and mean carrier lifetime ($\mu\tau$) is of great significance. This parameter represents the mean drifting distance of the carrier per unit of electric field before the carrier disappears due to recombination (or being trapped by defects) (Safa et al., 2011). To minimize the applied electric field, a large $\mu\tau$ is required. Lead halide perovskite has a large $\mu\tau$, ranging from 10^{-4} to 10^{-2} cm^2/(V·s), making it possible to attain high CCE under a low electric field (Wu et al., 2021).

3.2.2 Dark current

Dark current (I_d) is another parameter that determines the detection limit. Shot noise (i_n) is calculated as follows:

$$i_n = \sqrt{2eI_d\Delta f}, \tag{9}$$

where e is the elementary charge, and Δf is the bandwidth. Thus, a high dark current adversely affects the signal-to-noise ratio by increasing shot noise. In addition, a high dark current fills the storage capacitor and quickly reaches the breakdown voltage of TFT or complementary metal oxide semiconductor (CMOS) (Wu et al., 2021). Dark current is influenced by factors such as injected carriers and intrinsic thermally activated carriers. The injected carriers are closely related to the conductivity (σ) of the semiconductor material. Reducing conductivity is crucial for minimizing dark current. Since conductivity is determined by $\sigma=N_1e\mu$, where N_1 is the carrier concentration, one effective way to reduce conductivity is by lowering the carrier concentration. By using the Schottky structure, which can block the injection of carriers, Xu et al. (2020) successfully fabricated a $CsPbBr_3$ single crystal (SC) X-ray detector with low dark current density (about 5–27 nA/cm^2). The concentration of thermally activated carriers is related to the bandgap of the semiconductor. Wide bandgap semiconductors tend to have a low dark current. However, a broad bandgap contradicts the requirement that X-ray detectors need a narrow bandgap to achieve high sensitivity. So, it is necessary to choose a material with an appropriate bandgap to reduce the dark current and achieve high sensitivity.

3.2.3 Development of perovskite EIDs

In recent years, halide perovskites have gained extensive attention in the field of X-ray detection due to their strong X-ray stopping power and large $\mu\tau$ product.

Halide perovskite X-ray detectors were first demonstrated by Yakunin et al. (2015). Sensitivity reaching 25 μC/(mGy$_{air}$·cm^2) and responsivity of 1.9×10^4 carriers/photon were achieved using a solution-processed solar cell structure based on $MAPbI_3$ (MA is methylammonium). Huang et al. (2019) reported sensitive solution-processed $MAPbBr_3$ SC X-ray detectors with sensitivities of 80 μC/(Gy$_{air}$·cm^2) and a lowest detectable dose rate of 0.5 μGy$_{air}$/s (Wei et al., 2016). Further research by this group achieved a sensitivity of 2.1×10^4 μC/(Gy$_{air}$·cm^2) by monolithically integrating $MAPbBr_3$ SCs onto Si substrates (Wei W et al., 2017). Polycrystalline perovskites can also be used for direct X-ray detection. Shrestha et al. (2017) reported an X-ray detector made from sintered polycrystalline $MAPbI_3$ with a sensitivity of 2527 μC/(Gy$_{air}$·cm^2) at 0.2 V/μm electric field. Also in 2017, Sungkyunkwan University and Samsung reported the use of a thick film of $MAPbI_3$ perovskite based on the blade coating method combined with a TFT panel to realize large-area X-ray imaging (Kim et al., 2017). The device sensitivity of a single pixel reached 11000 μC/(Gy$_{air}$·cm^2). The device structure of the positive-intrinsic-negative (PIN) diode array is another consideration in EID design. A high sensitivity of 2.36×10^4 μC/(Gy$_{air}$·cm^2) was obtained based on an $MAPbBr_3$ PIN diode array (Wang et al., 2018). Ye et al. (2019) achieved a high sensitivity of 968.9 μC/(Gy$_{air}$·cm^2) under −1 V bias using cuboid $MAPbI_3$ SCs grown by the seed dissolution-regrowth method. Huang et al. (2019) further improved the performance of $MAPbI_3$ through A-site cation engineering. Large and flexible EIDs were demonstrated by mixing $MAPbI_3$ with a nylon membrane. The flexible detectors showed a high sensitivity of (8696±228) μC/(Gy$_{air}$·cm^2) (Zhao et al., 2020). Hu et al. (2020) then developed a heat-assisted press method for fabricating a large and compact perovskite wafer. A promising sensitivity of 1.22×10^5 μC/(Gy$_{air}$·cm^2) was achieved using an $MAPbI_3$ wafer.

Compared to organic-inorganic hybrid perovskites, all inorganic perovskites have emerged as highly promising materials due to their enhanced stability and superior X-ray absorption efficiency (Su et al., 2020). As early as 2013, Stoumpos et al. (2013) grew $CsPbBr_3$ SCs by the Bridgman method and predicted their potential for application in X-ray detection. In 2019, Pan et al. (2019) reported a $CsPbBr_3$ quasi-monocrystalline film made by hot pressing. X-ray EIDs using this kind of film achieved a sensitivity of 55684 μC/(Gy$_{air}$·cm^2). In the same year, Liu et al. (2019) synthesized $CsPbBr_3$ perovskite quantum dots (QDs) via a solution process, and devices made from $CsPbBr_3$ QDs attained a sensitivity up to 1450 μC/(Gy$_{air}$·cm^2). In 2021, a new low-temperature crystallization (LTC) method was developed by Peng et al. (2021). X-ray detectors fabricated from $CsPbBr_3$ that grew in water

through LTC reached a sensitivity of 4086 μC/(Gy_{air}·cm^2). Xue et al. (2023) used bromoacetic acid as an additive to increase the solubility of CsBr in dimethyl sulfoxide (DMSO). The $CsPbBr_3$ SCs grown from the additive-enhanced method reached a sensitivity of 3.0×10^4 μC/(Gy_{air}·cm^2). Pan et al. (2023) explored the performance of $CsPbBr_3$ EIDs under ultrahigh X-ray flux. The detector's photocurrent exhibited excellent linearity when the X-ray flux ranged from 10^6 to 10^{10} photons/(s·mm^2). To mitigate ion migration in EIDs based on $CsPbBr_3$, Zhang et al. (2022) doped iodine atoms into the melt-grown $CsPbBr_3$. The $CsPbBr_{2.9}I_{0.1}$ detector exhibited a high sensitivity of 6.3×10^4 μC/(Gy_{air}·cm^2) and a low detection limit of 54 nGy_{air}/s. Besides $CsPbBr_3$, $CsPbI_3$ can be used for X-ray detection. Zhang BB et al. (2020) reported X-ray detectors made from one-dimensional $CsPbI_3$ crystals.

The presence of Pb^{2+} in lead halide perovskites poses a significant risk to the human brain and biological systems due to its high solubility in water. Therefore, lead-free halide double perovskites have emerged as competitive materials for X-ray detectors. $Cs_2AgBiBr_6$ for X-ray detectors was first demonstrated in 2017 (Pan et al., 2017). Since the disordered arrangement of Ag^+/Bi^{3+} degrades the photoelectric properties of $Cs_2AgBiBr_6$ SCs, Yuan et al. (2019) used phenylethylamine bromide for in-situ regulation of the order-disorder phase transition in the $Cs_2AgBiBr_6$ SC. By controlling the crystal growth process of $Cs_2AgBiBr_6$ from the solubility and super solubility curves, Yin et al. (2019) successfully obtained $Cs_2AgBiBr_6$ SCs with high resistivity and considerable reproducibility. In addition to double perovskites, two-dimensional bismuth halide perovskites have attracted attention for their high performance in X-ray detection (Zhuang et al., 2019; Xia et al., 2020; Zhang YX et al., 2020; Wang et al., 2021; Li MB et al., 2022). Zhang et al. (2021) fabricated two-dimensional $Cs_3Bi_2Br_9$ SCs via the Bridgman method. The $Cs_3Bi_2Br_9$ SCs detector reached a sensitivity of 1705 μC/(Gy_{air}·cm^2) (Li X et al., 2022). Table 1 summarizes the device performances of traditional X-ray EIDs and perovskite X-ray EIDs.

Although halide perovskites are promising materials for X-ray detection, there are still some problems that need to be solved before they are applied commercially. Commercial flat-panel X-ray detectors need to have dark current densities below 1 nA/cm^2. The high dark current of perovskite X-ray EIDs greatly impedes their application in practical X-ray imaging. Therefore, a great effort has been made to suppress

Table 1 Key parameters and device performances of traditional X-ray EIDs and perovskite X-ray EIDs

Material	$\mu\tau$ product (cm^2/V)	Applied electric field (V/μm)	Sensitivity (μC/(Gy_{air}·cm^2))	Lowest detectable dose rate (nGy_{air}/s)	Reference
CdTe (P)	10^{-3} (e), 10^{-4} (h)	0.5	6.8×10^{-4}	–	del Sordo et al., 2009; Oh et al., 2014
CZT (S)	10^{-3}–10^{-2} (e), 10^{-5} (h)	0.1–1.0	318	5×10^4	Su et al., 2020; del Sordo et al., 2009
$MAPbBr_3$ (S) (PIN)	–	0.15	2.36×10^4	–	Wang et al., 2018
$MAPbI_3$ (S) (cuboid)	3.26×10^{-3} (h)	10^{-3}	968.9	–	Ye et al., 2019
$MAPbI_3$ (S) (GA alloyed)	1.25×10^{-2} (e)	–	2.3×10^4	16.9	Huang et al., 2019
MAPb $(I_{0.9}Cl_{0.1})_3$ (S) (flexible)	1.5×10^{-3} (e)	0.05	8696±228	–	Zhao et al., 2020
$MAPbI_3$ (wafer)	3.84×10^{-4} (e)	0.0125	1.22×10^5	–	Hu et al., 2020
$FA_{0.85}MA_{0.1}Cs_{0.05}PbI_{2.55}Br_{0.45}$ (S)	1.72×10^{-3} (e)	0.06	$(3.5\pm0.2)\times10^6$	42	Liu et al., 2021
$CsPbBr_3$ (P)	1.32×10^{-2} (e)	–	55684	215	Pan et al., 2019
$CsPbBr_3$ (QD)	–	~5	1450	–	Liu et al., 2019
$CsPbI_3$ (1D)	3.63×10^{-3} (e)	4.17×10^{-3}	2370	219	Zhang BB et al., 2020
$Cs_2AgBiBr_6$ (S)	6.3×10^{-3} (e)	2.5×10^{-3}	105	59.7	Pan et al., 2017
$Cs_2AgBiBr_6$ (S)	1.94×10^{-3} (e)	0.0227	288.8	–	Yuan et al., 2019
$Cs_2AgBiBr_6$ (S)	5.95×10^{-3} (e)	0.05	1974	45.7	Yin et al., 2019
$(F\text{-}PEA)_3BiI_6$ (2D)	4×10^{-4} (lateral), 8.3×10^{-5} (vertical)	0.1	118.6 (lateral), 52.6 (vertical)	1800 (lateral), 30 (vertical)	Pan et al., 2017

P: polycrystal; S: single crystal; e: electron; h: hole; FA: formamidinium; PEA: phenethylamine

the dark current of perovskite X-ray EIDs. Zhou et al. (2021) exploited heterojunction structures to reduce dark current in perovskite X-ray EIDs. A wide band-gap perovskite layer was inserted between the regular perovskite and the electrode, effectively blocking the hole and electron injection (Figs. 3a and 3b). The dark current of the heterojunction device was 200 times lower than that of the single junction device

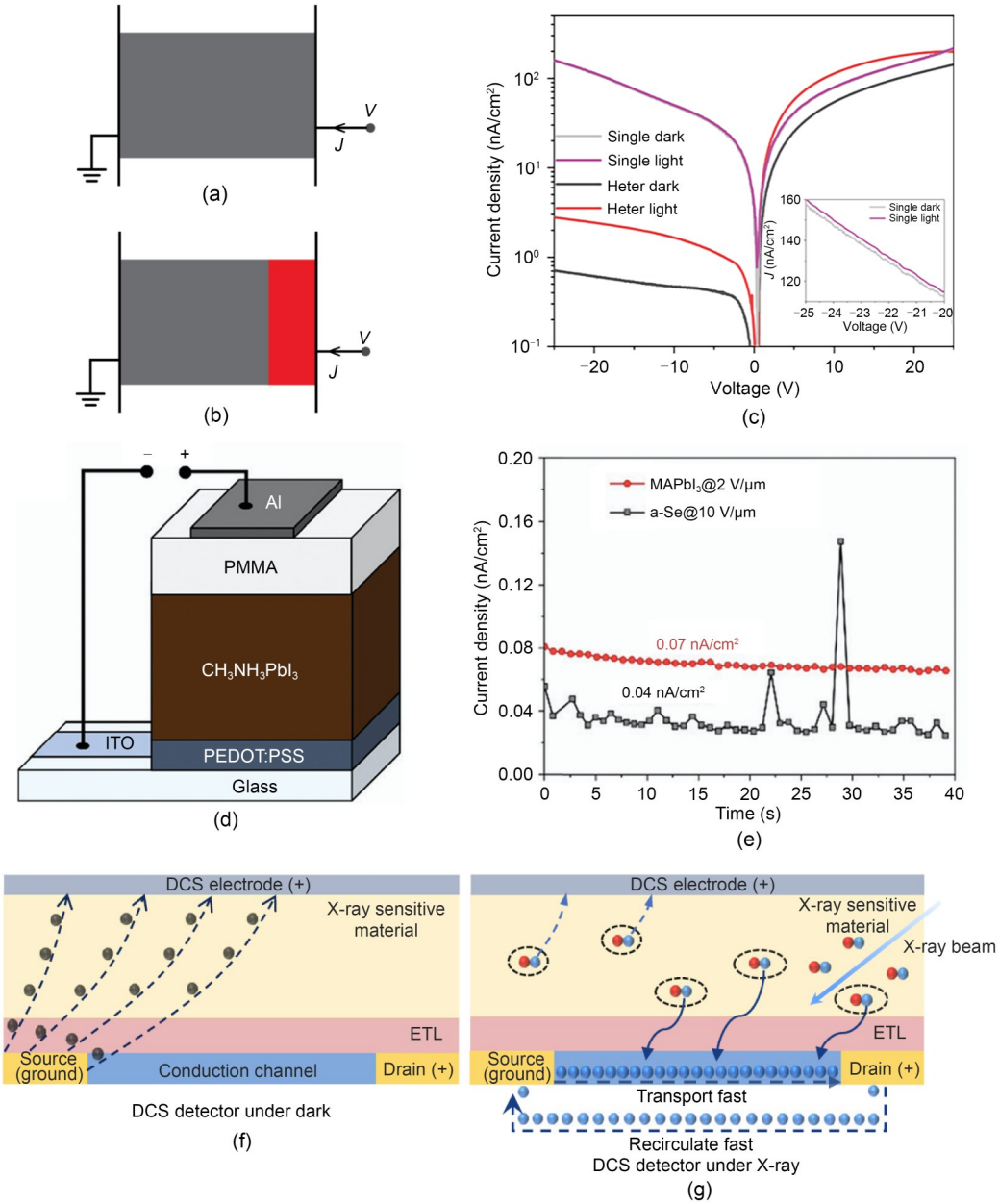

Fig. 3 (a) Schematic of a single junction device (*J* is the current density); (b) Schematic of heterojunction device; (c) Device performance of single junction and heterojunction device; (d) Schematic diagram of the PMMA inserted EIDs (ITO is the indium tin oxide, and PEDOT:PSS is the poly(3,4-ethylenedioxythiophene):poly(styrenesulfonate)); (e) Dark current density of $MAPbI_3$ EIDs and a-Se EIDs; (f) Working mechanism of dark-current-shunting (DCS) detector under dark (ETL is the electron transport layer); (g) Working mechanism of DCS detector under X-ray. Part of the X-ray induced electrons transport into the conduction channel to generate electrical signal. Figs. 3a–3c are reprinted from (Zhou et al., 2021), Copyright 2021, with permission from American Association for the Advancement of Science. Figs. 3d and 3e are reprinted from (Li YL et al., 2022), Copyright 2022, with permission from Royal Society of Chemistry. Figs. 3f and 3g are reprinted from (Jin et al., 2023), Copyright 2023, with permission from Springer Nature. References to color refer to the online version of this figure

(Fig. 3c). Another way to reduce dark current is to introduce an insulated polymer layer. By inserting a polymethyl methacrylate (PMMA) layer between $MAPbI_3$ and the electrode, Li YL et al. (2022) achieved a low dark current density of 70 pA/cm^2, which was comparable to that of a-Se X-ray EIDs (Figs. 3d and 3e). In conventional EIDs, the dark current and photocurrent are conducted in the same path and collected by the same electrode. Thus, reducing dark current inevitably results in lower photocurrent. To address this problem, Jin et al. (2023) introduced a third electrode called a dark-current-shunting electrode to collect dark current. The photocurrent is collected by a drain electrode (Figs. 3d and 3f). Through this strategy, Jin et al. (2023) achieved a record dark current of 51.1 fA.

Ion migration is another problem that degrades the performance of perovskite EIDs. Ion migration not only limits the charge extraction in the detector but also launches electrochemical reactions that lead to the irreversible degradation of the material. In 2021, Liu et al. (2021) successfully grew $FAPbI_3$ SC (FAMACs SC) with not only MA and Cs cations but also Br anions incorporated into the $FAPbI_3$ lattice. Ion migration in FAMACs SCs was effectively suppressed and X-ray EIDs made of FAMACs SCs demonstrated a high sensitivity of $(3.5\pm0.2)\times10^6$ μC/(Gy_{air}·cm^2). Heterojunctions are also considered an effective method to suppress ion migration. By exploiting a facile solution-based epitaxial method, Zhang et al. (2023) fabricated $MAPbBr_3$/$MAPbI_3$ heterojunctions with a sensitivity of 3.98×10^5 μC/(Gy_{air}·cm^2) and a low detection limit of 12.2 nGy_{air}/s. The ion migration activation energy of a heterojunction (0.47 eV) is higher than those of $MAPbBr_3$ SCs (0.24 eV) and $MAPbI_3$ SCs (0.35 eV).

3.3 Photon counting detectors (PCDs)

PCDs work in voltage mode (Fig. 2c) and are used mainly for spectroscopy. Unlike EIDs, PCDs operate at a relatively low X-ray dose. The X-ray photons reach the detector one by one. Each incident photon generates a number of electron-hole pairs that produce an electrical signal. The intensity of the signal pulse is proportional to the energy of the X-ray photon. An application-specific integrated circuit (ASIC) records the number of incident photons and discriminates the energy of each photon. Fig. 2d provides a detailed illustration of the ASIC. The input signal pulse is amplified by a preamplifier and reshaped by a shaper. Next, the intensity of the input signal is compared in several comparators, which are always between 2 and 8, each with a different preset threshold. If the intensity exceeds the threshold, the corresponding counter counts the signal once. Subtracting the counts from two counters allows the determination of the number of photons within the specified threshold range.

PCDs have several advantages over EIDs. First, EIDs integrate the total energy deposited in the detectors, so the output signal inevitably consists of a small amount of noise. In contrast, PCDs can effectively eliminate noise by setting the lowest energy threshold higher than the noise. Consequently, PCDs can enable new low-dose imaging protocols at dose levels where electronic noise is prohibitive with state-of-the-art scanners (Danielsson et al., 2021). Even though PCDs can mitigate counting noise, the noise still affects the signal intensity and results in inaccurate energy. Secondly, low-energy photons carry more contrast information than high-energy photons (Danielsson et al., 2021). In EIDs, the output signal relies on the total energy deposited in the detectors. Therefore, high-energy photons contribute more to the output signal, which may cause degradation of the image contrast. In contrast, photons with different energies contribute equally to the output signals of PCDs. As a result, PCDs can attain a higher image contrast than EIDs. However, PCDs still pose numerous challenges that impede their commercial application.

3.3.1 Pulse pileup

Pulse pileup occurs in all kinds of PCDs since thousands of photons are incident in the PCDs in a short time interval. If two photons arrive at the PCDs almost simultaneously, the signal pulses will superimpose, leading to false counts. Two types of pulse pileup are depicted in Figs. 4a and 4b. In Fig. 4a, two signal pulses overlap each other and create a new pulse. The PCDs not only lose counts but also count the photons with incorrect energy. In Fig. 4b, the time interval between the two signal pulses is slightly larger than that in Fig. 4a. The PCDs might record them as two separate counts, but the recorded energies of the two photons are incorrect. Pulse pileup results in image quality degradation in two respects. Firstly, the

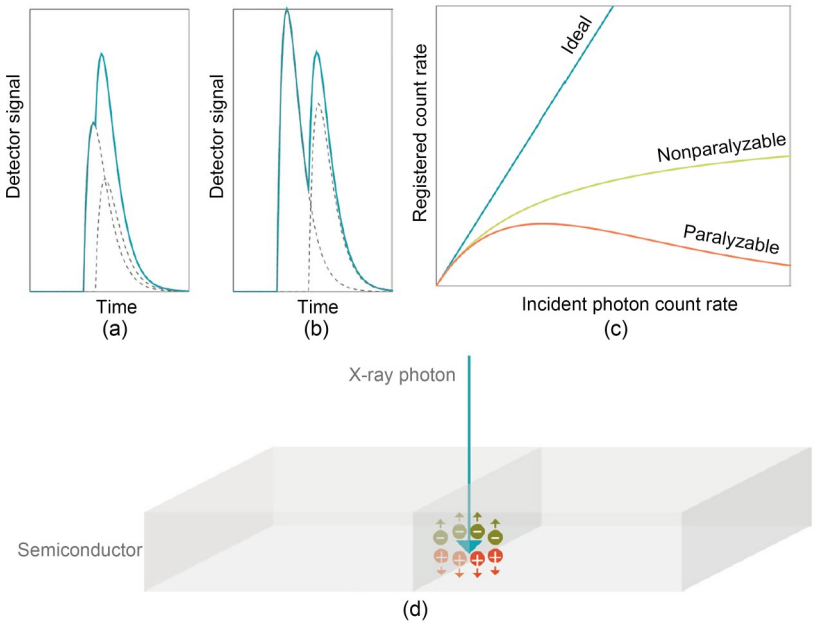

Fig. 4 (a) Schematic of the first type of pulse pileup (two signals superimpose on each other and the PCD counts them as one count); (b) Schematic of the second type of pulse pileup (two signals superimpose on each other and the PCD counts them as two counts with incorrect energy); (c) Relationship between registered count rate and incident photon count rate for three different kinds of PCDs; (d) Schematic of charge sharing (charge sharing occurs when the generated electron-hole pairs are near the pixel boundaries; a fraction of electron-hole pairs is absorbed by the adjacent pixels, resulting in inaccurate counts or count loss). Reprinted from (Willemink et al., 2018), Copyright 2018, with permission from Radiological Society of North American

loss of counts increases image noise because fewer photons contribute to the measurement (Alvarez, 2014). Secondly, the energy resolution decreases, leading to increased image noise.

The pulse pileup is closely related to the count rate of PCDs. Fig. 4c illustrates that ideal PCDs, without the pulse pileup effect, exhibit a registered count rate equal to the incident photon count rate. However, due to the pulse pileup effect, the registered count rate is lower than the incident photon count rate. For a nonparalyzable PCD, it gradually saturates and reaches a limit value. For a paralyzable PCD, the registered count rate drops after reaching the maximum registered count rate. Alleviating the pulse pileup effect requires PCDs to have a short charge collection time. Therefore, semiconductors with high carrier mobility are desirable. Additionally, it is crucial to minimize the thickness of the semiconductor layer to reduce charge transport time while ensuring complete X-ray absorption. As a consequence, semiconductors with a high average atomic number are needed. Perovskite materials, with considerable carrier mobility and a relatively high atomic number, emerge as a potential solution to mitigate the pulse pileup effect.

3.3.2 Charge sharing

The charge sharing effect is almost unavoidable in PCDs because the radiation semiconductor is electrically, rather than physically, pixelated (Ren et al., 2018). Each incident photon generates multiple electron-hole pairs (Fig. 4d). If the electron-hole pairs are located near the pixel boundaries, there is a high probability that the neighboring pixels will absorb a fraction of the electron-hole pairs. Charge sharing in PCDs can result in three possible effects. First, one incident photon might be counted twice if the pulse intensities of both pixels exceed the lowest threshold. The energy of these two counts is lower than the real energy of the incident photon. Second, one incident photon might be counted once with the registered energy lower than its actual energy if the pulse intensity of the adjacent pixel is below the lowest threshold. Third, PCDs may lose a count if both pulse intensities are below the lowest threshold.

There are several factors affecting the probability of charge sharing. High-energy incident photons generate more electron-hole pairs, resulting in a higher likelihood of charge sharing. Pixel size is also related

to charge sharing. The electron-hole pairs are more likely to be generated near the pixel boundaries for small-size pixels. Therefore, charge sharing is more prevalent in PCDs with small pixels. The impacts of carrier mobility and thickness of the semiconductor layer on charge sharing are similar to their effects on pulse pileup. Semiconductor materials, which have high carrier mobility and high atomic number to reduce the thickness of the active layer, can mitigate the charge sharing effect.

3.3.3 Progress in the development of PCDs

Materials widely used for PCDs include CdTe, CZT, and silicon. Given the significantly higher atomic numbers of CdTe and CZT, their linear absorption coefficients are several times greater than that of silicon. The typical thicknesses of CdTe or CZT range from 0.9 to 3.0 mm (Barber et al., 2013; Taguchi and Iwanczyk, 2013). To attain a high detection efficiency, PCDs based on silicon must increase the thickness of the detector. Silicon wafers need a thickness of 30 mm to achieve a detection efficiency of about 80% (Taguchi, 2017). Nevertheless, fabricating silicon wafers thicker than a few millimeters is currently impossible (Danielsson et al., 2021), but the length of the silicon wafers could be sufficient to ensure high detection efficiency. Consequently, the device configuration of silicon-based PCDs is different from that of CdTe or CZT-based PCDs. Silicon-based PCDs use an edge-on geometry design while CdTe or CZT-based PCDs use a face-on geometry (Figs. 5a and 5b). Fig. 5c shows the detector module of edge-on silicon PCDs. The module consists of 50 strips, each divided into 16 segments (Xu et al., 2013).

In recent years, perovskite materials have also attracted interest for their potential for making PCDs. Edge-on geometry was first used for an energy resolved perovskite X-ray detector by Pang et al. (2022). The relationship between the incident X-ray spectrum and the detector signal can be calculated using the following equation:

$$\boldsymbol{C}_{m\times m}^{-1}\cdot\boldsymbol{R}_{m\times 1}=\boldsymbol{S}_{m\times 1}, \tag{10}$$

where $\boldsymbol{C}_{m\times m}^{-1}$ is the inverse matrix of the conversion matrix, $\boldsymbol{R}_{m\times 1}$ is the detector signal, and $\boldsymbol{S}_{m\times 1}$ is the incident X-ray spectrum (Pang et al., 2022). By altering the incident X-ray spectrum, $\boldsymbol{C}_{m\times m}^{-1}$ can be obtained

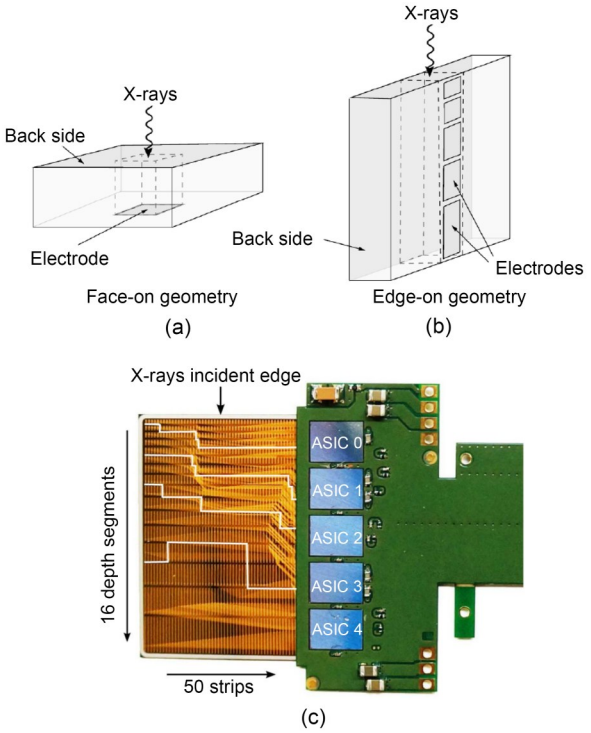

Fig. 5 (a) Schematic of face-on PCDs (X-rays are incident on the backside); (b) Schematic of the edge-on PCDs (X-rays are incident on the edge of silicon); (c) Edge-on silicon PCD with 50 strips and 16 segments. Figs. 5a and 5b are reprinted from (Danielsson et al., 2021), Copyright 2021, with permission from IOP Publishing. Fig. 5c is reprinted from (Xu et al., 2013), Copyright 2013, with permission from Elsevier

using machine learning. Pang et al. (2022) selected $MAPbBr_3$ SC as the semiconductor layer. Each electrode has a different thickness to ensure that it produces a similar amplitude of signals (Fig. 6a). Fig. 6b depicts the simulated X-ray spectra and the reconstructed spectrum when the X-ray tube was driven at voltages of 45, 55, and 65 kVp. To further testify the performance of this energy resolved perovskite X-ray detector, Pang et al. (2022) used it to detect an artificial sample. The images from the 2nd and 5th electrodes are shown in Figs. 6c and 6e, respectively. The image from the 2nd electrode contains more low-energy X-ray photons, whereas the image from the 5th electrode contains more high-energy X-ray photons (Pang et al., 2022). The images of the high-density $CaCO_3$ tablet and low-density paraffin 'H' letter can be obtained by different subtraction algorithms (Figs. 6d and 6f).

Studies of perovskite PCDs with a face-on geometry have focused mainly on γ-ray detection. The first

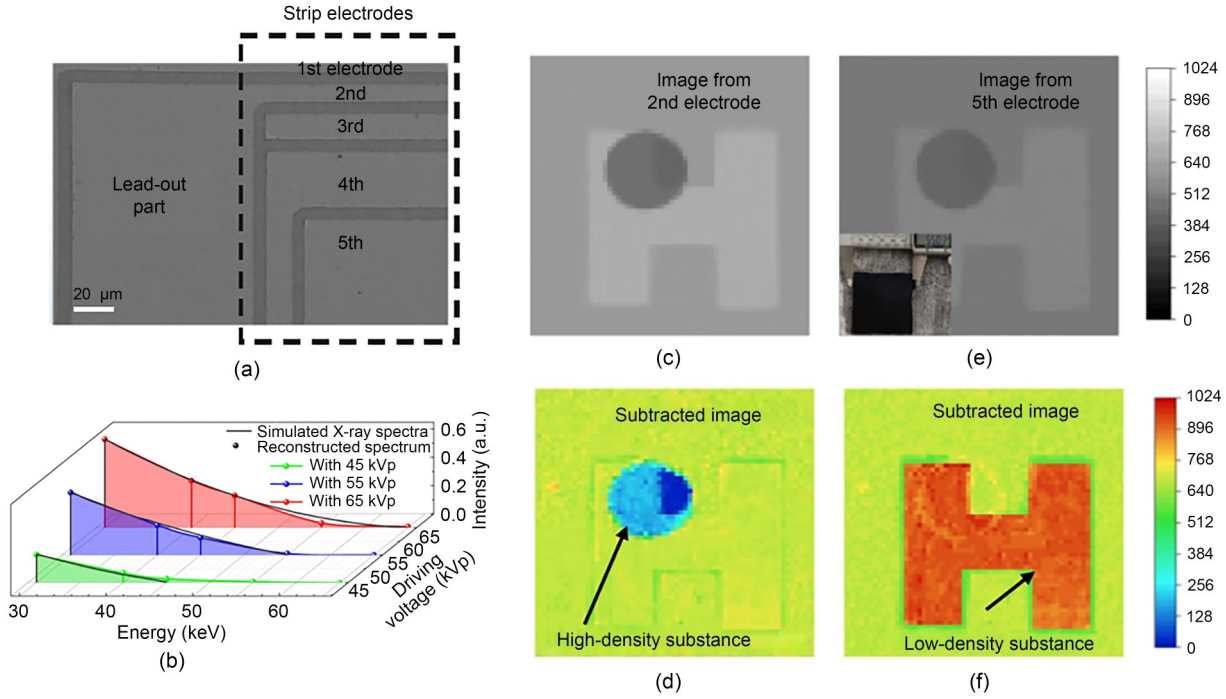

Fig. 6 (a) Scanning electron microscope photo of strip electrodes; (b) Simulated X-ray spectra and reconstructed spectrum when the driving voltages of the X-ray tube were 45, 55, and 65 kVp; (c) Image of the artificial sample from the 2nd electrode; (d) Subtracted image of a high-density substance $CaCO_3$ tablet; (e) Image of the artificial sample from the 5th electrode; (f) Subtracted image of a low-density substance paraffin 'H' letter. Reprinted from (Pang et al., 2022), Copyright 2022, with permission from Springer Nature. References to color refer to the online version of this figure

demonstration of perovskite γ-ray detectors was implemented through $FAPbI_3$ with a 35% energy resolution for 662 keV γ-rays (Yakunin et al., 2016). However, black α-$FAPbI_3$ SCs exhibit thermodynamic instability, because they convert into a wide-bandgap δ-phase, inhibiting the device's long-term use (Yakunin et al., 2016). To address this issue, researchers from the same group conducted further studies. Quinary $Cs_xFA_{1-x}PbI_{3-y}Br_y$ (x=0.0–0.1 and y=0.0–0.6) was fabricated by incorporating Cs and Br into the lattice of $FAPbI_3$ (Nazarenko et al., 2017). This improved the duration of stable work from about two weeks for black α-$FAPbI_3$ to four months. MA-based perovskites exhibit higher phase stability and better performance for γ-ray detection than FA-based perovskites (Liu et al., 2022). Wei HT et al. (2017) synthesized high quality and dopant-compensated $MAPbBr_{2.94}Cl_{0.06}$ and obtained an energy resolution of 12% at 662 keV γ-rays using this kind of perovskite SC. He et al. (2018b) reported a Schottky-type $MAPbI_3$ γ-ray detector. The device achieved an energy resolution of 6.8% for ^{57}Co 122 keV γ-rays on account of the high $\mu\tau$ product. Tisdale et al. (2020) investigated the performance of $MAPbBr_{2.85}Cl_{0.15}$. They observed an unusually slow rise time and a poor energy resolution of about 25% for 662 keV γ-rays, which they attributed to low charge trapping and de-trapping, ion migration, and charge accumulation (Tisdale et al., 2020).

Similar to their advantages in EIDs, all-inorganic perovskites exhibit improved device performance in PCDs. He et al. (2018a) reported a $CsPbBr_3$ γ-ray detector with a high energy resolution of 3.8% for 662 keV γ-rays. The improved crystal growth method, incorporating a specially designed device configuration featuring asymmetrical electrode materials, contributed significantly to achieving this high energy resolution (He et al., 2018a). The solution growth method for $CsPbBr_3$ is more cost-effective than the Bridgman method. Pan et al. (2020) reported a γ-ray detector made of solution-processed $CsPbBr_3$ SCs with an energy resolution of 5.5% for 662 keV γ-rays. He et al. (2021a) reported a groundbreaking achievement in $CsPbBr_3$ perovskite γ-ray detection, achieving an exceptional energy resolution of 1.4% for 662 keV γ-rays, which is the best energy resolution for γ-ray

detectors achieved so far. $CsPbCl_3$ is another competitive perovskite for γ-ray detection. He et al. (2021b) demonstrated the possibility of using $CsPbCl_3$ for γ-ray detection, with an energy resolution of about 16% for 122 keV γ-rays. Double perovskites such as $Cs_2AgBiBr_6$ (Zhang et al., 2021) and perovskite-related materials ($A_3B_2X_9$) (Mccall et al., 2018) also show a promising future for energy-resolved γ-ray detection.

An X-ray energy-resolved perovskite detector was recently demonstrated by He et al. (2022). A Schottky device with a Bi/$CsPbBr_3$/Au configuration was used (Fig. 7a). Device performance was tested using γ-rays (^{109}Cd source) and X-rays (Ag X-ray tube). Because of the single-photon nature of the γ-ray source, the measured γ-ray spectrum was free of pile-up. In contrast, the measured X-ray spectrum underwent severe pulse pile-up because the count rates were limited and multiple photons impinged on the detector in a short time interval. Sakhatskyi et al. (2023) demonstrated energy-resolved X-ray imaging using $MAPbI_3$ SC detectors (Fig. 7b). The detector reached a detection efficiency of 88% and a noise-equivalent dose of 90 pGy_{air} with 18 keV X-rays (Sakhatskyi et al., 2023). Table 2 summarizes the device performances of perovskite γ-ray and X-ray PCDs.

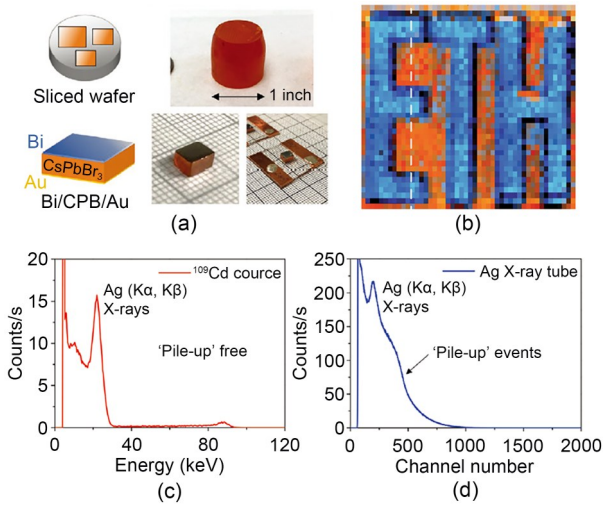

Fig. 7 (a) Wafer grown from Bridgman method and device configuration of $CsPbBr_3$; (b) Energy-resolved image of the characters 'ETH'; (c) Spectrum of the ^{109}Cd source measured by the $CsPbBr_3$ detector; (d) Spectrum of the Ag X-ray tube measured by the $CsPbBr_3$ detector. Figs. 7a, 7c, and 7d are reprinted from (He et al., 2022), Copyright 2022, with permission from John Wiley & Sons, Inc. Fig. 7b is reprinted from (Sakhatskyi et al., 2023), Copyright 2023, with permission from Springer Nature

4 Summary and outlook

Halide perovskites have emerged as promising materials for EIDs and PCDs owing to their superior photoelectric properties. Compared with the widely used materials such as silicon, a-Se, and CZT for radiation detection, halide perovskites offer advantages including strong X-ray stopping power, large $\mu\tau$ product, low dark current, high sensitivity, and cost-effective fabrication. The sensitivity of perovskite-based EIDs has significantly increased, from 80 μC/(Gy_{air}·cm^2) of an $MAPbBr_3$ EID to (3.5±0.2)×10^5 μC/(Gy_{air}·cm^2) of an FAMACs EID. Halide perovskite PCDs have also undergone rapid development in recent years. The energy resolution of the first $FAPbI_3$ PCD was 35% for 662 keV γ-rays. The highest achieved energy resolution is 1.4% for 662 keV γ-rays using a $CsPbBr_3$ perovskite γ-ray detector. Despite significant breakthroughs, the use of halide perovskites for radiation

Table 2 Key parameters and device performances of perovskite γ-ray and X-ray PCDs

Material	$\mu\tau$ product (cm^2/V)	Applied electric field	Source	Energy resolution (%)	Reference
$FAPbI_3$	1.8×10^{-2}	7.7×10^{-3} V/μm	^{241}Am	35	Yakunin et al., 2016
$MAPbBr_{2.94}Cl_{0.06}$	1.8×10^{-2}	1.8×10^{-3} V/μm	^{137}Cs	12	Wei HT et al., 2017
$MAPbI_3$	8.1×10^{-4} (h), 7.4×10^{-4} (e)	4.6×10^{-2} V/μm	^{57}Co	6.8	He et al., 2018b
$CsPbBr_3$	1.34×10^{-3} (h), 8.77×10^{-4} (e)	1.667 V/μm	^{137}Cs	3.8	He et al., 2018a
$CsPbBr_3$	4×10^{-4}	–	^{137}Cs	5.5	Pan et al., 2020
$CsPbBr_3$	8×10^{-3} (h)	500 V	^{137}Cs	1.4	He et al., 2021a
$CsPbCl_3$	3.2×10^{-4} (h)	300 V	^{57}Co	~16	He et al., 2021b
$Cs_2AgBiBr_6$	1.47×10^{-3}	6.67×10^{-2} V/μm	^{241}Am	13.91	Zhang et al., 2021
$CsPbBr_3$	3×10^{-3}	–	Ag	~24	He et al., 2022

detection still faces several challenges that limit their practical application.

The long-term performance of perovskite radiation detectors, particularly organic-inorganic perovskites, remains a challenge. The organic cation of organic-inorganic perovskites typically decomposes when the temperature reaches 60 °C (Brunetti et al., 2016). Additionally, organic-inorganic perovskites face challenges related to ion migration, leading to hysteresis and phase segregation (Yuan and Huang, 2016). Device performance frequently experiences degradation within a few hours of operation. Therefore, there is an urgent need to enhance the prolonged performance of perovskite radiation detectors.

The solution growth method is more cost-effective than the Bridgman method for synthesizing halide perovskites but the device performance of solution-processed perovskites is inferior (Liu et al., 2022). Therefore, additional research is needed to fabricate high-quality single crystals using the solution growth method.

Lead-free halide perovskites have attracted much attention because they eliminate the risk of Pb toxicity. However, the performance of lead-free double perovskites and two-dimensional perovskites still falls far short of the theoretical limit. Perovskite-related materials ($A_3B_2X_9$) suitable for energy-resolved detectors have not yet been demonstrated. Hence, more efforts are needed to explore lead-free halide perovskites.

X-ray PCDs have the capability to resolve the energy of incident photons, allowing the recording of X-ray images with a higher signal-to-noise ratio and improved resolution. However, perovskite X-ray PCDs suffer from ion migration that originates from their electronic-ionic nature. Ion migration can have detrimental effects on device performance, leading to large dark current and a reduction in long-term operating stability. Strategies must be devised to suppress ion migration, a pervasive issue in perovskite materials. Photon fluxes used for clinical diagnosis reach as high as 10^6 to 10^9 photons/(s·mm^2). Perovskite X-ray PCDs may encounter pulse pile-up that can result in count loss under such a high photon flux. Consequently, perovskite X-ray PCDs with a high count rate are essential for clinical use. Further improvement in energy resolution is also needed to obtain higher-resolution X-ray images.

Acknowledgments

This work is supported by the Outstanding Youth Fund of the National Natural Science Foundation of China (No. T2325020), the National Natural Science Foundation of China (Nos. 62074136 and 52273307), and the Natural Science Foundation of Zhejiang Province, China (No. LZ23F050005).

Author contributions

Yibin LAI wrote the first draft of the manuscript. Yang (Michael) YANG helped to organize the manuscript and revised the final version.

Conflict of interest

Yibin LAI and Yang (Michael) YANG declare that they have no conflict of interest.

References

Alvarez RE, 2014. Signal to noise ratio of energy selective X-ray photon counting systems with pileup. *Medical Physics*, 41(11):111909. https://doi.org/10.1118/1.4898102

Als-Nielsen J, McMorrow D, 2011. Elements of Modern X-ray Physics. 2nd Edition. John Wiley & Sons, Inc., USA.

Barber WC, Wessel JC, Nygard E, et al., 2013. High flux energy-resolved photon-counting X-ray imaging arrays with CdTe and CdZnTe for clinical CT. The 3rd International Conference on Advancements in Nuclear Instrumentation, Measurement Methods and Their Applications (ANIMMA). https://doi.org/10.1109/ANIMMA.2013.6728030

Brunetti B, Cavallo C, Ciccioli A, et al., 2016. On the thermal and thermodynamic (in)stability of methylammonium lead halide perovskites. *Scientific Reports*, 6(1):31896. https://doi.org/10.1038/srep31896

Danielsson M, Persson M, Sjölin M, 2021. Photon-counting X-ray detectors for CT. *Physics in Medicine & Biology*, 66(3):03TR01. https://doi.org/10.1088/1361-6560/abc5a5

del Sordo S, Abbene L, Caroli E, et al., 2009. Progress in the development of CdTe and CdZnTe semiconductor radiation detectors for astrophysical and medical applications. *Sensors*, 9(5):3491-3526. https://doi.org/10.3390/s90503491

Devanathan R, Corrales LR, Gao F, et al., 2006. Signal variance in gamma-ray detectors—a review. *Nuclear Instruments and Methods in Physics Research Section A: Accelerators, Spectrometers, Detectors and Associated Equipment*, 565(2):637-649. https://doi.org/10.1016/j.nima.2006.05.085

Evans RD, Beiser A, 1956. The atomic nucleus. *Physics Today*, 9(12):33-34. https://doi.org/10.1063/1.3059850

Guerra M, Manso M, Longelin S, et al., 2012. Performance of three different Si X-ray detectors for portable XRF

spectrometers in cultural heritage applications. *Journal of Instrumentation*, 7(10):C10004. https://doi.org/10.1088/1748-0221/7/10/C10004

He YH, Matei L, Jung HJ, et al., 2018a. High spectral resolution of gamma-rays at room temperature by perovskite $CsPbBr_3$ single crystals. *Nature Communications*, 9(1): 1609. https://doi.org/10.1038/s41467-018-04073-3

He YH, Ke WJ, Alexander GCB, et al., 2018b. Resolving the energy of γ-ray photons with $MAPbI_3$ single crystals. *ACS Photonics*, 5(10):4132-4138. https://doi.org/10.1021/acsphotonics.8b00873

He YH, Petryk M, Liu ZF, et al., 2021a. $CsPbBr_3$ perovskite detectors with 1.4% energy resolution for high-energy γ-rays. *Nature Photonics*, 15(1):36-42. https://doi.org/10.1038/s41566-020-00727-1

He YH, Stoumpos CC, Hadar I, et al., 2021b. Demonstration of energy-resolved γ-ray detection at room temperature by the $CsPbCl_3$ perovskite semiconductor. *Journal of the American Chemical Society*, 143(4):2068-2077. https://doi.org/10.1021/jacs.0c12254

He YH, Hadar I, de Siena MC, et al., 2022. Sensitivity and detection limit of spectroscopic-grade perovskite $CsPbBr_3$ crystal for hard X-ray detection. *Advanced Functional Materials*, 32(24):2112925. https://doi.org/10.1002/adfm.202112925

Hendee W, 2010. Radiation physics for medical physicists—2nd ed. *Medical Physics*, 37(9):5148. https://doi.org/10.1118/1.3481669

Hu MX, Jia SS, Liu YC, et al., 2020. Large and dense organic–inorganic hybrid perovskite $CH_3NH_3PBI_3$ wafer fabricated by one-step reactive direct wafer production with high X-ray sensitivity. *ACS Applied Materials & Interfaces*, 12(14):16592-16600. https://doi.org/10.1021/acsami.9b23158

Huang YM, Qiao L, Jiang YZ, et al., 2019. A-site cation engineering for highly efficient $MAPbI_3$ single-crystal X-ray detector. *Angewandte Chemie International Edition*, 58(49): 17834-17842. https://doi.org/10.1002/anie.201911281

Jin P, Tang YD, Li DW, et al., 2023. Realizing nearly-zero dark current and ultrahigh signal-to-noise ratio perovskite X-ray detector and image array by dark-current-shunting strategy. *Nature Communications*, 14(1):626. https://doi.org/10.1038/s41467-023-36313-6

Kainz K, 2006. Radiation oncology physics: a handbook for teachers and students. *Medical Physics*, 33(6Part1):1920. https://doi.org/10.1118/1.2201870

Kalaga DV, Kulkarni AV, Acharya R, et al., 2009. Some industrial applications of gamma-ray tomography. *Journal of the Taiwan Institute of Chemical Engineers*, 40(6): 602-612. https://doi.org/10.1016/j.jtice.2009.05.012

Kasap SO, 2000. X-ray sensitivity of photoconductors: application to stabilized a-Se. *Journal of Physics D: Applied Physics*, 33(21):2853-2865. https://doi.org/10.1088/0022-3727/33/21/326

Kim HS, Lee CR, Im JH, et al., 2012. Lead iodide perovskite sensitized all-solid-state submicron thin film mesoscopic solar cell with efficiency exceeding 9%. *Scientific Reports*, 2(1):591. https://doi.org/10.1038/srep00591

Kim J, Jung SH, Moon J, et al., 2012. Development of transportable gamma-ray tomographic system for industrial application. *Nuclear Instruments and Methods in Physics Research Section A: Accelerators, Spectrometers, Detectors and Associated Equipment*, 693:203-208. https://doi.org/10.1016/j.nima.2012.07.046

Kim YC, Kim KH, Son DY, et al., 2017. Printable organometallic perovskite enables large-area, low-dose X-ray imaging. *Nature*, 550(7674):87-91. https://doi.org/10.1038/nature24032

Kojima A, Teshima K, Shirai Y, et al., 2009. Organometal halide perovskites as visible-light sensitizers for photovoltaic cells. *Journal of the American Chemical Society*, 131(17): 6050-6051. https://doi.org/10.1021/ja809598r

Leroy C, Rancoita PG, 2011. Principles of Radiation Interaction in Matter and Detection. 3rd Edition. World Scientific, Singapore. https://doi.org/10.1142/8200

Li MB, Li HY, Li WJ, et al., 2022. Oriented 2D perovskite wafers for anisotropic X-ray detection through a fast tableting strategy. *Advanced Materials*, 34(8):2108020. https://doi.org/10.1002/adma.202108020

Li X, Zhang P, Hua YQ, et al., 2022. Ultralow detection limit and robust hard X-ray imaging detector based on inch-sized lead-free perovskite $Cs_3Bi_2Br_9$ single crystals. *ACS Applied Materials & Interfaces*, 14(7):9340-9351. https://doi.org/10.1021/acsami.1c24086

Li YL, Adeagbo E, Koughia C, et al., 2022. Direct conversion X-ray detectors with 70 pA cm^{-2} dark currents coated from an alcohol-based perovskite ink. *Journal of Materials Chemistry C*, 10(4):1228-1235. https://doi.org/10.1039/D1TC05338H

Lin EC, 2010. Radiation risk from medical imaging. *Mayo Clinic Proceedings*, 85(12):1142-1146. https://doi.org/10.4065/mcp.2010.0260

Liu FZ, Wu R, Wei J, et al., 2022. Recent progress in halide perovskite radiation detectors for gamma-ray spectroscopy. *ACS Energy Letters*, 7(3):1066-1085. https://doi.org/10.1021/acsenergylett.2c00031

Liu JY, Shabbir B, Wang CJ, et al., 2019. Perovskite X-ray detectors: flexible, printable soft-X-ray detectors based on all-inorganic perovskite quantum dots (Adv. Mater. 30/2019). *Advanced Materials*, 31(30):1970214. https://doi.org/10.1002/adma.201970214

Liu YC, Zhang YX, Zhu XJ, et al., 2021. Triple-cation and mixed-halide perovskite single crystal for high-performance X-ray imaging. *Advanced Materials*, 33(8):2006010. https://doi.org/10.1002/adma.202006010

Mccall KM, Liu ZF, Trimarchi G, et al., 2018. α-particle detection and charge transport characteristics in the $A_3M_2I_9$ defect perovskites (A = Cs, Rb; M = Bi, Sb). *ACS Photonics*, 5(9):3748-3762. https://doi.org/10.1021/acsphotonics.8b00813

Nazarenko O, Yakunin S, Morad V, et al., 2017. Single crystals of caesium formamidinium lead halide perovskites: solution growth and gamma dosimetry. *NPG Asia Materials*, 9(4):e373. https://doi.org/10.1038/am.2017.45

Oh KM, Kim DK, Shin JW, et al., 2014. Measurement of the electrical properties of a polycrystalline cadmium telluride for direct conversion flat panel X-ray detector. *Journal of Instrumentation*, 9(1):P01010. https://doi.org/10.1088/1748-0221/9/01/P01010

Pan L, Feng YX, Kandlakunta P, et al., 2020. Performance of perovskite $CsPbBr_3$ single crystal detector for gamma-ray detection. *IEEE Transactions on Nuclear Science*, 67(2): 443-449. https://doi.org/10.1109/TNS.2020.2964306

Pan L, Liu ZF, Welton C, et al., 2023. Ultrahigh-flux X-ray detection by a solution-grown perovskite $CsPbBr_3$ single-crystal semiconductor detector. *Advanced Materials*, 35(25):2211840. https://doi.org/10.1002/adma.202211840

Pan WC, Wu HD, Luo JJ, et al., 2017. $Cs_2AgBiBr_6$ single-crystal X-ray detectors with a low detection limit. *Nature Photonics*, 11(11):726-732. https://doi.org/10.1038/s41566-017-0012-4

Pan WC, Yang B, Niu GD, et al., 2019. Hot-pressed $CsPbBr_3$ quasi-monocrystalline film for sensitive direct X-ray detection. *Advanced Materials*, 31(44):1904405. https://doi.org/10.1002/adma.201904405

Pang JC, Zhao S, Du XY, et al., 2022. Vertical matrix perovskite X-ray detector for effective multi-energy discrimination. *Light: Science & Applications*, 11(1):105. https://doi.org/10.1038/s41377-022-00791-y

Peng JL, Xia CQ, Xu YL, et al., 2021. Crystallization of $CsPbBr_3$ single crystals in water for X-ray detection. *Nature Communications*, 12(1):1531. https://doi.org/10.1038/s41467-021-21805-0

Ren LQ, Zheng B, Liu H, 2018. Tutorial on X-ray photon counting detector characterization. *Journal of X-Ray Science and Technology*, 26(1):1-28. https://doi.org/10.3233/XST-16210

Rothwarf A, 1973. Plasmon theory of electron-hole pair production: efficiency of cathode ray phosphors. *Journal of Applied Physics*, 44(2):752-756. https://doi.org/10.1063/1.1662257

Safa S, Frey JB, Belev G, et al., 2011. Amorphous and polycrystalline photoconductors for direct conversion flat panel X-ray image sensors. *Sensors*, 11(5):5112-5117. https://doi.org/10.3390/s110505112

Sakhatskyi K, Turedi B, Matt GJ, et al., 2023. Stable perovskite single-crystal X-ray imaging detectors with single-photon sensitivity. *Nature Photonics*, 17(6):510-517. https://doi.org/10.1038/s41566-023-01207-y

Shrestha S, Fischer R, Matt GJ, et al., 2017. High-performance direct conversion X-ray detectors based on sintered hybrid lead triiodide perovskite wafers. *Nature Photonics*, 11(7):436-440. https://doi.org/10.1038/nphoton.2017.94

Spahn M, 2013. X-ray detectors in medical imaging. *Nuclear Instruments and Methods in Physics Research Section A: Accelerators, Spectrometers, Detectors and Associated Equipment*, 731:57-63. https://doi.org/10.1016/j.nima.2013.05.174

Stoumpos CC, Malliakas CD, Peters JA, et al., 2013. Crystal growth of the perovskite semiconductor $CsPbBr_3$: a new material for high-energy radiation detection. *Crystal Growth & Design*, 13(7):2722-2727. https://doi.org/10.1021/cg400645t

Su YR, Ma WB, Yang Y, 2020. Perovskite semiconductors for direct X-ray detection and imaging. *Journal of Semiconductors*, 41(5):38-47. https://doi.org/10.1088/1674-4926/41/5/051204

Taguchi K, 2017. Energy-sensitive photon counting detector-based X-ray computed tomography. *Radiological Physics and Technology*, 10(1):8-22. https://doi.org/10.1007/s12194-017-0390-9

Taguchi K, Iwanczyk JS, 2013. Vision 20/20: single photon counting X-ray detectors in medical imaging. *Medical Physics*, 40(10):100901. https://doi.org/10.1118/1.4820371

Tan ZK, Moghaddam RS, Lai ML, et al., 2014. Bright light-emitting diodes based on organometal halide perovskite. *Nature Nanotechnology*, 9(9):687-692. https://doi.org/10.1038/nnano.2014.149

Thompson M, Ellison SLR, Wood R, 2002. Harmonized guidelines for single-laboratory validation of methods of analysis (IUPAC technical report). *Pure and Applied Chemistry*, 74(5):835-855. https://doi.org/doi:10.1351/pac200274050835

Tisdale JT, Yoho M, Tsai H, et al., 2020. Methylammonium lead tribromide single crystal detectors towards robust gamma-ray photon sensing. *Advanced Optical Materials*, 8(10):2000233. https://doi.org/10.1002/adom.202000233

van Eijk CWE, 2002. Inorganic scintillators in medical imaging. *Physics in Medicine & Biology*, 47(8):R85. https://doi.org/10.1088/0031-9155/47/8/201

Wang CF, Li HJ, Li MG, et al., 2021. Centimeter-sized single crystals of two-dimensional hybrid iodide double perovskite $(4,4\text{-difluoropiperidinium})_4AgBiI_8$ for high-temperature ferroelectricity and efficient X-ray detection. *Advanced Functional Materials*, 31(13):2009457. https://doi.org/10.1002/adfm.202009457

Wang X, Zhao DW, Qiu YP, et al., 2018. PIN diodes array made of perovskite single crystal for X-ray imaging. *Physica Status Solidi: Rapid Research Letters*, 12(10):1800380. https://doi.org/10.1002/pssr.201800380

Wei HT, Huang JS, 2019. Halide lead perovskites for ionizing radiation detection. *Nature Communications*, 10(1):1066. https://doi.org/10.1038/s41467-019-08981-w

Wei HT, Fang YJ, Mulligan P, et al., 2016. Sensitive X-ray detectors made of methylammonium lead tribromide perovskite single crystals. *Nature Photonics*, 10(5):333-339. https://doi.org/10.1038/nphoton.2016.41

Wei HT, Desantis D, Wei W, et al., 2017. Dopant compensation in alloyed $CH_3NH_3PbBr_{3-x}Cl_x$ perovskite single crystals

for gamma-ray spectroscopy. *Nature Materials*, 16(8): 826-833.
https://doi.org/10.1038/nmat4927

Wei W, Zhang Y, Xu Q, et al., 2017. Monolithic integration of hybrid perovskite single crystals with heterogenous substrate for highly sensitive X-ray imaging. *Nature Photonics*, 11(5):315-321.
https://doi.org/10.1038/nphoton.2017.43

Willemink MJ, Persson M, Pourmorteza A, et al., 2018. Photon-counting CT: technical principles and clinical prospects. *Radiology*, 289(2):293-312.
https://doi.org/10.1148/radiol.2018172656

Wu HD, Ge YS, Niu GD, et al., 2021. Metal halide perovskites for X-ray detection and imaging. *Matter*, 4(1): 144-163.
https://doi.org/10.1016/j.matt.2020.11.015

Xia M, Yuan JH, Niu G, et al., 2020. Unveiling the structural descriptor of $A_3B_2X_9$ perovskite derivatives toward X-ray detectors with low detection limit and high stability. *Advanced Functional Materials*, 30(24):1910648.
https://doi.org/10.1002/adfm.201910648

Xing GC, Mathews N, Lim SS, et al., 2014. Low-temperature solution-processed wavelength-tunable perovskites for lasing. *Nature Materials*, 13(5):476-480.
https://doi.org/10.1038/nmat3911

Xu C, Chen H, Persson M, et al., 2013. Energy resolution of a segmented silicon strip detector for photon-counting spectral CT. *Nuclear Instruments and Methods in Physics Research Section A: Accelerators, Spectrometers, Detectors and Associated Equipment*, 715:11-17.
https://doi.org/10.1016/j.nima.2013.02.030

Xu Q, Wang X, Zhang H, et al., 2020. $CsPbBr_3$ single crystal X-ray detector with schottky barrier for X-ray imaging application. *ACS Applied Electronic Materials*, 2(4):879-884.
https://doi.org/10.1021/acsaelm.9b00832

Xue ZX, Wei YR, Li H, et al., 2023. Additive-enhanced crystallization of inorganic perovskite single crystals for high-sensitivity X-ray detection. *Small*, 19(18):2207588.
https://doi.org/10.1002/smll.202207588

Yakunin S, Sytnyk M, Kriegner D, et al., 2015. Detection of X-ray photons by solution-processed lead halide perovskites. *Nature Photonics*, 9(7):444-449.
https://doi.org/10.1038/nphoton.2015.82

Yakunin S, Dirin DN, Shynkarenko Y, et al., 2016. Detection of gamma photons using solution-grown single crystals of hybrid lead halide perovskites. *Nature Photonics*, 10(9): 585-589.
https://doi.org/10.1038/nphoton.2016.139

Ye F, Lin H, Wu HD, et al., 2019. High-quality cuboid $CH_3NH_3PbI_3$ single crystals for high performance X-ray and photon detectors. *Advanced Functional Materials*, 29(6):1806984.
https://doi.org/10.1002/adfm.201806984

Yin LX, Wu HD, Pan WC, et al., 2019. Controlled cooling for synthesis of $Cs_2AgBiBr_6$ single crystals and its application for X-ray detection. *Advanced Optical Materials*, 7(19): 1900491.
https://doi.org/10.1002/adom.201900491

Yuan WN, Niu GD, Xian YM, et al., 2019. In situ regulating the order–disorder phase transition in $Cs_2AgBiBr_6$ single crystal toward the application in an X-ray detector. *Advanced Functional Materials*, 29(20):1900234.
https://doi.org/10.1002/adfm.201900234

Yuan YN, Huang JS, 2016. Ion migration in organometal trihalide perovskite and its impact on photovoltaic efficiency and stability. *Accounts of Chemical Research*, 49(2):286-293.
https://doi.org/10.1021/acs.accounts.5b00420

Zentai G, 2008. X-ray imaging for homeland security. IEEE International Workshop on Imaging Systems and Techniques, p.1-6.
https://doi.org/10.1109/IST.2008.4659929

Zhang BB, Liu X, Xiao B, et al., 2020. High-performance X-ray detection based on one-dimensional inorganic halide perovskite $CsPbI_3$. *The Journal of Physical Chemistry Letters*, 11(2):432-437.
https://doi.org/10.1021/acs.jpclett.9b03523

Zhang P, Hua YQ, Xu YD, et al., 2022. Ultrasensitive and robust 120 keV hard X-ray imaging detector based on mixed-halide perovskite $CsPbBr_{3-n}I_n$ single crystals. *Advanced Materials*, 34(12):2106562.
https://doi.org/10.1002/adma.202106562

Zhang XJ, Chu DP, Jia BX, et al., 2023. Heterointerface design of perovskite single crystals for high-performance X-ray imaging. *Advanced Materials*, 36(3):2305513.
https://doi.org/10.1002/adma.202305513

Zhang YX, Liu YC, Xu Z, et al., 2020. Nucleation-controlled growth of superior lead-free perovskite $Cs_3Bi_2I_9$ single-crystals for high-performance X-ray detection. *Nature Communications*, 11(1):2304.
https://doi.org/10.1038/s41467-020-16034-w

Zhang Z, Cao D, Huang ZJ, et al., 2021. Gamma-ray detection using Bi-poor $Cs_2AgBiBr_6$ double perovskite single crystals. *Advanced Optical Materials*, 9(8):2001575.
https://doi.org/10.1002/adom.202001575

Zhao JJ, Zhao L, Deng YH, et al., 2020. Perovskite-filled membranes for flexible and large-area direct-conversion X-ray detector arrays. *Nature Photonics*, 14(10):612-617.
https://doi.org/10.1038/s41566-020-0678-x

Zhou Y, Zhao L, Ni ZY, et al., 2021. Heterojunction structures for reduced noise in large-area and sensitive perovskite X-ray detectors. *Science Advances*, 7(36):eabg6716.
https://doi.org/10.1126/sciadv.abg6716

Zhuang RZ, Wang XJ, Ma WB, et al., 2019. Highly sensitive X-ray detector made of layered perovskite-like $(NH_4)_3Bi_2I_9$ single crystal with anisotropic response. *Nature Photonics*, 13(9):602-608.
https://doi.org/10.1038/s41566-019-0466-7